

# Hierarchical Structure of CuO Nanowires Decorated with Ni(OH)<sub>2</sub> Supported on Cu Foam for Hydrogen Production via Urea Electrocatalysis

Hainan Sun, Jiapeng Liu, Gao Chen, Hyunseung Kim, Sangwoo Kim, Zhiwei Hu, Jin-Ming Chen, Shu-Chih Haw, Francesco Ciucci,\* and WooChul Jung\*

Owing to the low theoretical potential of the urea oxidation reaction (UOR), urea electrolysis is an energy-saving technique for the generation of hydrogen. Herein, a hierarchical structure of CuO nanowires decorated with nickel hydroxide supported on 3D Cu foam is constructed. Combined theoretical and experimental analyses demonstrate the high reactivity and selectivity of CuO and Ni(OH)<sub>2</sub> toward the UOR instead of the oxygen evolution reaction. The hierarchical structure creates a synergistic effect between the two highly active sites, enabling an exceptional UOR activity with a record low potential of 1.334 V (vs the reversible hydrogen electrode) to reach 100 mA cm<sup>-2</sup> and a low Tafel slope of 14 mV dec<sup>-1</sup> in 1 M KOH and 0.5 M urea electrolyte. Assembling full urea electrolysis driven by this developed UOR electrocatalyst as the anode and a commercial Pt/C electrocatalyst as the cathode provides a current density of 20 mA cm<sup>-2</sup> at a cell voltage of ≈1.36 V with promising operational stability for at least 150 h. This work not only enriches the UOR material family but also significantly advances energy-saving hydrogen production.

overpotentials are required to drive water splitting in practical applications, mainly due to the kinetically unfavorable rate of the anodic reaction, that is, the oxygen evolution reaction (OER).<sup>[3]</sup> Compared with the other half-reaction (hydrogen evolution reaction (HER)), OER, which involves four-electron-transfer processes to form oxygen–oxygen bonds, is considered to be the bottleneck for the overall water splitting.<sup>[4]</sup> To overcome this drawback, replacing water molecules with more oxidizable molecules, such as urea, ethanol, amine, and hydrazine, paves another route to energy-saving hydrogen production.<sup>[5]</sup> In particular, compared with the traditional water oxidation reaction, the urea oxidation reaction (UOR; CO(NH<sub>2</sub>)<sub>2</sub> + 6OH<sup>-</sup> → N<sub>2</sub> + 5H<sub>2</sub>O + CO<sub>2</sub> + 6e<sup>-</sup>) requires an ultralow theoretical voltage (0.37 V vs RHE).<sup>[6]</sup>

Thus, assisted by the anodic UOR, urea electrolysis (CO(NH<sub>2</sub>)<sub>2</sub> + H<sub>2</sub>O → 3H<sub>2</sub> + N<sub>2</sub> + CO<sub>2</sub>) is a promising technique that can produce hydrogen in an energy-saving manner.<sup>[6a]</sup> Moreover, UOR-based urea electrolysis also is an avenue to realize urea-rich industrial and agricultural wastewater purification.<sup>[6a]</sup> Of note, the kinetics of UOR is also sluggish due to the involved six-electron-transfer process.<sup>[7]</sup> Therefore, considerable attention has been devoted to designing a UOR catalyst that is cost-effective and high active while being durable for long periods of time.

## 1. Introduction

Efficient hydrogen production technologies will enable the transition from a fossil-fuel economy to a clean and sustainable hydrogen economy, and electrochemical water splitting (2H<sub>2</sub>O → 2H<sub>2</sub> + O<sub>2</sub>) is of great interest as a key process for producing high-purity hydrogen without a carbon footprint.<sup>[1]</sup> The theoretical potential for water electrolysis is 1.23 V (vs reversible hydrogen electrode (RHE)).<sup>[2]</sup> However, large

H. Sun, H. Kim, S. Kim, W. Jung  
Department of Materials Science and Engineering  
Korea Advanced Institute of Science and Technology (KAIST)  
Daejeon 34141, Republic of Korea  
E-mail: wcjung@kaist.ac.kr

J. Liu, F. Ciucci  
Department of Mechanical and Aerospace Engineering  
The Hong Kong University of Science and Technology  
Kowloon, Hong Kong 999077, P. R. China  
E-mail: francesco.ciucci@ust.hk

 The ORCID identification number(s) for the author(s) of this article can be found under <https://doi.org/10.1002/smt.202101017>.

DOI: 10.1002/smt.202101017

G. Chen  
Department of Building and Real Estate  
The Hong Kong Polytechnic University  
Hung Hom, Kowloon, Hong Kong 999077, P. R. China

Z. Hu  
Max Planck Institute for Chemical Physics of Solids  
01187 Dresden, Germany

J.-M. Chen, S.-C. Haw  
National Synchrotron Radiation Research Center  
Hsinchu 30076, Taiwan

F. Ciucci  
Department of Chemical and Biological Engineering  
The Hong Kong University of Science and Technology  
Kowloon, Hong Kong, P. R. China

First-row transition metals of Fe, Co, and Ni with flexible valence states and spin states exhibit high intrinsic catalytic activity for the OER and UOR.<sup>[3f,4a,8]</sup> Considerable attention has been focused on designing high-performance Fe-, Co-, and Ni-based single-metal and multimetal materials as alternatives to noble-metal-based materials.<sup>[6a,9]</sup> In particular, Ni-based materials are considered as UOR electrocatalysts under alkaline conditions.<sup>[6b,9b,10]</sup> Nickel sulfides, nickel phosphides, and nickel (oxy)hydroxides directly grown on conductive substrates are the most representative state-of-the-art materials for the UOR.<sup>[11]</sup> Of note, Ni-based electrocatalysts can also serve as active materials for the OER (a competitive side reaction compared to UOR). Thus, the competition between the OER and UOR determines the chemoselectivity of the electrocatalyst during the catalytic process.<sup>[12]</sup> Despite many research efforts, the report about Ni-based UOR catalysts that achieved sufficiently high activity, selectivity, and durability is still limited. Consequently, there is a need for a comprehensive understanding of materials' selection and reaction mechanisms, along with research on new materials to replace Ni. Here, we select nickel hydroxide (Ni(OH)<sub>2</sub>), a class of 2D materials, as a proof of concept to investigate the UOR behaviors.<sup>[3g,13]</sup> Additionally, we take Cu, another inexpensive transition metal (Co: 32.8 USD kg<sup>-1</sup> and Cu: 6.0 USD kg<sup>-1</sup>), as a potential candidate for material designs.<sup>[14]</sup> It has been demonstrated that high-valence metal sites are active for the OER and UOR.<sup>[4a,6a,7c]</sup> Compared to Co, Fe, and Ni, Cu shows relatively fewer types of valence states.<sup>[11f,15]</sup> During the oxidation reaction conditions, Cu<sup>2+</sup> ions can be referred to as high-valence metal sites in the system of Cu ions (Cu<sup>0+</sup>, Cu<sup>1+</sup>, and Cu<sup>2+</sup>). This indicates that Cu<sup>2+</sup>-based materials may also be promising for the OER or UOR, which is dependent on the adsorption features during these reaction processes.<sup>[7a]</sup> Moreover, the electrocatalytic activities of reported Cu-based materials toward the OER and UOR (e.g., metallic Cu, Cu sulfides, Cu phosphides, Cu oxide, and Cu (oxy)hydroxides) have much room to be further improved to meet the requirements of practical applications. Therefore, a systematic evaluation of Cu-based materials from both theoretical and experimental points of view is highly desirable.

In addition, a high-performance electrocatalyst that can be widely used should be characterized by having a large amount of active sites, high conductivity, and sufficient stability against corrosion reaction conditions (e.g., in situ formation of active species from a conductive substrate and/or design binder-free electrodes).<sup>[16]</sup> Rationally integrating two active species is an effective approach to achieve a synergistic effect that can realize the ultimate goal of improving electrocatalytic activity and stability.<sup>[17]</sup> Therefore, constructing a self-supporting electrode with a hierarchical structure containing considerable amounts of exposed highly active sites also satisfies the aforementioned requirements.

Herein, we designed a hierarchical structure containing CuO nanowires (NWs) and Ni(OH)<sub>2</sub> through wet chemical oxidation followed by a low-temperature treatment and electrodeposition process. The in situ formed CuO NWs supported on conductive Cu foam (CF) with a 3D open structure enable substantial exposure of active surface sites and easy accessibility of reactants, as well as high electrical conductivity for charge transfer. Combined density functional theory (DFT) calculations and

experimental analyses demonstrate that CuO and Ni(OH)<sub>2</sub> possess high electrocatalytic activity and selectivity toward the UOR rather than the OER. Rational construction of a hierarchical structure also results in a synergistic effect between two highly active sites. Impressively, the optimized electrode exhibits an exceptional UOR activity with an ultralow potential of 1.334 V (vs RHE) to reach 100 mA cm<sup>-2</sup> and a low Tafel slope of 14 mV dec<sup>-1</sup> in 1 M KOH and 0.5 M urea electrolyte, outperforming reported state-of-the-art UOR electrocatalysts. Furthermore, full urea electrolysis can provide 20 mA cm<sup>-2</sup> at a low cell voltage of ≈1.36 V (0.13 V lower than that of a traditional water electrolyzer) with promising operational stability. This work highlights the remarkable potential of constructing 3D copper-nickel-based nanostructured materials as efficient and low-cost electrocatalysts for the UOR to advance energy-saving hydrogen production.

## 2. Results and Discussion

High-valence metal sites have been demonstrated as highly active species for the OER and UOR.<sup>[4a,6a,7b]</sup> First-row transition metal elements of Co, Fe, and Ni display flexible valence states and spin states. For instance, Co elements have multivalence states ranging from Co<sup>0</sup> to Co<sup>4+</sup> along with various spin states such as low-, intermediate-, and high-spin states.<sup>[18]</sup> However, Cu ions show fewer types of valence states, commonly including Cu<sup>0+</sup>, Cu<sup>1+</sup>, and Cu<sup>2+</sup>.<sup>[19]</sup> We first try to unravel the effect of Cu ion states on OER and UOR behaviors in an alkaline environment through DFT calculations. The constructed structural models for the calculations are shown in **Figure 1a–c**, and related details can be found in the Supporting Information.

Based on the reaction mechanisms, the OH<sup>-</sup> and urea adsorption is the first step of the OER and UOR processes, respectively.<sup>[4a,7a,20]</sup> Moreover, it was reported that the catalyst-urea state, which can be effectively reflected by the adsorption energy, has a significant effect on the onset potential of urea oxidation.<sup>[20,21]</sup> Thus, DFT calculations were first carried out for urea and OH<sup>-</sup> adsorbed on the CuO (111) surface. As depicted in **Figure 1d**, the adsorption energy of urea onto CuO (111) is almost six times higher than that of OH<sup>-</sup> on CuO (111) surface (−0.98 vs −0.18 eV), indicating that CuO (111) favors the adsorption of urea, which may contribute to superior UOR selectivity. To further understand the role of Cu<sup>2+</sup> for the UOR, the adsorption energy values of urea onto the Cu<sup>0+</sup> (111) and Cu<sub>2</sub><sup>1+O</sup> (111) surfaces were also compared, and the values follow the order of CuO (111) > Cu<sub>2</sub>O (111) > Cu (111) (**Figure 1e**). Notably, the adsorption values on CuO (111) are ≈2.1-fold and ≈2.7-fold greater than the values on Cu<sub>2</sub>O (111) and Cu (111), respectively, implying that higher-valence Cu<sup>2+</sup> is more active for the UOR. Additionally, low-valence transition-metal ions are prone to be oxidized into high-valence states under oxidation reaction conditions.<sup>[4a]</sup> The possible phase transition of Cu<sub>2</sub>O and Cu during the UOR process will be evaluated in the following sections. In short, Cu<sup>2+</sup> has the highest valence state and is expected to be stable as highly active sites during the electrochemical reaction toward the UOR.

Additionally, 2D nanomaterials exhibit the characteristics of highly exposed catalytic active sites on the surface and superior

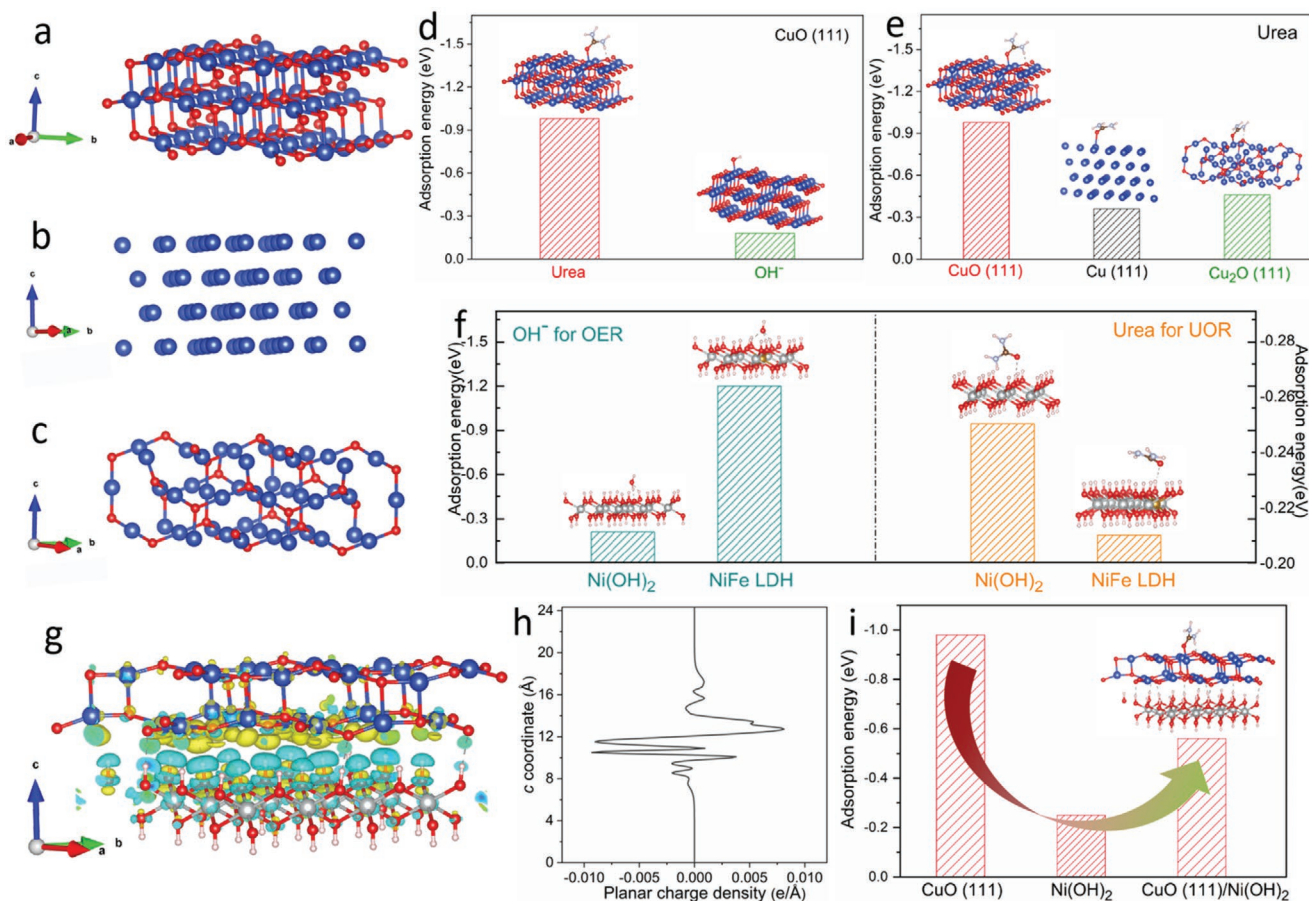


**Figure 1.** The structural models of a) CuO (111), b) Cu (111), and c) Cu<sub>2</sub>O (111) for urea and/or OH<sup>-</sup> adsorption (Cu: blue and O: red). d) Adsorption energy of urea and OH<sup>-</sup> on CuO (111) surface. e) Adsorption energy of urea on Cu (111), Cu<sub>2</sub>O (111), and CuO (111) surfaces. f) Adsorption energy of urea and OH<sup>-</sup> on Ni(OH)<sub>2</sub> and NiFe LDH. g) Atomistic model of the CuO (111)/Ni(OH)<sub>2</sub> heterostructure with a charge density difference plot, in which the cyan and yellow colors represent electron loss and gain, respectively. h) The planar average charge density difference along the *c*-direction. i) The comparison of adsorption energies of urea on CuO (111), Ni(OH)<sub>2</sub>, and CuO (111)/Ni(OH)<sub>2</sub> surface models.

electron transportation ability.<sup>[22]</sup> In particular, the Ni-based hydroxide is one of the most promising 2D materials applied in electrochemical conversion reactions.<sup>[13b,c]</sup> Here, we employed Ni(OH)<sub>2</sub> and NiFe layered double hydroxide (NiFe LDH) as a proof of concept to showcase the advantages of Ni-based materials toward the UOR. To illustrate the electrocatalysis process toward UOR and OER, the adsorption energies of urea and OH<sup>-</sup> on Ni(OH)<sub>2</sub> and NiFe LDH (Figure S1, Supporting Information) were calculated. As shown in Figure 1f, NiFe LDH exhibits a much larger adsorption energy toward OH<sup>-</sup> (-1.2 eV) than that of Ni(OH)<sub>2</sub> (-0.25 eV), indicating favorable adsorption toward the OER of NiFe LDH. This characteristic is consistent with the high OER activity of NiFe LDH in alkaline media reported previously.<sup>[23]</sup> In contrast, a favorable adsorption feature of Ni(OH)<sub>2</sub> toward UOR is demonstrated by the large value of adsorption energy of urea (Figure 1f). Therefore, Ni(OH)<sub>2</sub> is expected to show higher UOR activity than that of NiFe LDH. More importantly, rationally integrating two active species can be an effective approach to achieve a synergy that can realize the ultimate goal of improving electrocatalytic activity and selectivity. To understand the interplay between CuO and Ni(OH)<sub>2</sub>, we constructed a model consisting of CuO (111) and Ni(OH)<sub>2</sub>

by stacking along the *c*-direction (Figure S2, Supporting Information). The calculated charge difference plot for the heterostructure of CuO (111)/Ni(OH)<sub>2</sub> is shown in Figure 1g, in which a transfer of electrons from the Ni(OH)<sub>2</sub> to the CuO (111) can be observed. This is also consistent with the planar average charge difference density as shown in Figure 1h, where a positive (negative) charge above (below) the heterointerface ( $\approx 12$  Å) is noticed, verifying the electron transfer from Ni(OH)<sub>2</sub> to the CuO (111), as well as the synergistic interaction between the two substrates. Additionally, the adsorption energies for urea and OH<sup>-</sup> at the heterostructure have been calculated on both the CuO (111) and the Ni(OH)<sub>2</sub> side. It was demonstrated that the urea prefers to be adsorbed on the top of the CuO (111) side with an adsorption energy of -0.56 eV (Figure 1i), whereas the OH<sup>-</sup> prefers to be adsorbed at the Ni(OH)<sub>2</sub> side with an energy of -0.45 eV (Figure S3, Supporting Information). The intermediate adsorption behavior of urea on the heterostructure may imply a decreased activation barrier in the following reaction steps compared to the pure CuO (111) (Figure 1i). On the other hand, the energy is strong enough to assure the adsorption of urea on the heterostructure than on the pure Ni(OH)<sub>2</sub> (Figure 1i).

The basic requirements for high-performance electrocatalysts include a considerable level of active species on the surface, high electrical conductivity favorable for charge transfer, and sufficient stability. Meanwhile, in order to obtain the advantage of CuO's high activity, we constructed a self-supported complex electrode in which CuO NWs were spontaneously coated on the surface of a commercial CF through chemical oxidation and calcination processes (Figure 2a).<sup>[11f,23a,24]</sup> Specifically, the commercial CF with a 3D network serves as both the conductive substrate and Cu source for the growth of vertically oriented Cu(OH)<sub>2</sub> NWs through the reported chemical oxidation process (for more details on the synthesis process, please refer to the "Experimental Section" in the Supporting Information).<sup>[11f,23a,25]</sup> Cu(OH)<sub>2</sub> NWs/CF was then calcined in air (180 °C for 1 h) to obtain CuO NWs/CF. Electrodeposition has been demonstrated as a facile and effective method to deposit 2D materials on substrates.<sup>[9d,11f,13c,23a,24–26]</sup> Finally, ultrathin Ni(OH)<sub>2</sub> nanosheets were electrodeposited on the surface of the CuO NWs/CF in a Ni(NO<sub>3</sub>)<sub>2</sub> aqueous solution, giving rise to the generation of a self-supported electrode containing CF-supported hierarchical Ni(OH)<sub>2</sub>/CuO NWs' nanostructure (denoted as Ni(OH)<sub>2</sub>/CuO NWs/CF) (Figure 2a).

The surface morphological and structural features of the obtained materials were first examined by field emission scanning electron microscopy (FE-SEM). Commercial CF has a smooth surface and exhibits a 3D open structure (Figure 2b; Figure S4, Supporting Information). After the alkaline corrosion process, uniform 1D nanowire morphologies of Cu(OH)<sub>2</sub> NWs were found to be vertically oriented on the CF surface (Figure S5, Supporting Information). Through the calcination process in an air atmosphere, Cu(OH)<sub>2</sub> was then transformed into CuO. As shown in Figure 2c and in Figure S6 (Supporting Information), CuO NWs still exhibit 1D structures with uniform size, which facilitates further coating process. Compared to the needle-like structure of Cu(OH)<sub>2</sub> NWs, the surface of CuO NWs becomes relatively rough. Finally, CuO NWs/CF prepared in this way acts as a scaffold for subsequent electrodeposition, and, as a result, a thin Ni(OH)<sub>2</sub> layer is uniformly coated on the surface. Importantly, Ni(OH)<sub>2</sub>/CuO NWs/CF retains the nanowire structure with a small amount of self-aggregation (Figure 2d; Figure S7, Supporting Information). Transmission electron microscope (TEM) and high-resolution TEM (HRTEM) images further confirmed the successful formation of CuO and Ni(OH)<sub>2</sub>, and provided more microstructural details. The lattice fringe with an interplanar distance of 0.232 nm could be indexed well to the (111) plane of CuO, verifying the generation of CuO on the Cu substrate as observed from the X-ray diffraction (XRD) pattern (Figure 2e). Uniform nanowire morphologies with an average diameter of ≈140 nm and uniformly distributed Cu and O elements were also found (Figure S8, Supporting Information). After electrodeposition treatment, the well-retained nanowire structure of CuO is displayed in TEM images (Figure 2f). A distinctive lattice fringe with an interplanar spacing of 0.24 nm can be assigned to the (101) plane of Ni(OH)<sub>2</sub> (Figure 2g).<sup>[3g]</sup> The high-angle annular dark field-scanning transmission electron microscopy (HAADF-STEM) and corresponding energy dispersive X-ray (EDX) elemental mapping images were captured as well, demonstrating the coexistence of Ni, Cu, and O elements and the uniform distribution of these elements (Figure 2h). The EDX scanning reveals that the Ni(OH)<sub>2</sub>/CuO NWs/CF contains a small

content of Ni element (≈0.8 wt% of the total elements; Figure S9, Supporting Information).

The crystal phases of the materials were further studied by XRD data. Figure 2i shows the typical XRD patterns for CF, Cu(OH)<sub>2</sub> NWs/CF, and CuO NWs/CF. The surface-cleaned CF exhibits three strong and sharp peaks at 2θ of 43.2°, 50.4°, and 74.1°, corresponding to metallic Cu (PDF#04–0836).<sup>[11f,23a]</sup> An orthorhombic Cu(OH)<sub>2</sub> phase (PDF#35–0505) was identified after the chemical oxidation process, which was completely transformed into a CuO phase (PDF#48–1548) by calcination in an air atmosphere.<sup>[27]</sup> The XRD patterns of Ni(OH)<sub>2</sub>/CuO NWs/CF, taken after the deposition of Ni(OH)<sub>2</sub> over CuO NWs/CF, demonstrated low intensity for Ni(OH)<sub>2</sub>, mainly owing to the low concentration of Ni(OH)<sub>2</sub> and peaks overlapping between Ni(OH)<sub>2</sub> and CuO (Figure S10, Supporting Information).<sup>[27]</sup> As the next step, we determined the valence states of Ni ions and Cu ions at the surface of the Ni(OH)<sub>2</sub>/CuO NWs/CF sample. For this purpose, we used the surface-sensitive soft X-ray absorption spectroscopy (sXAS) spectra at the Cu-L<sub>2,3</sub> and the Ni-L<sub>2,3</sub> edges collected with a total electron yield (TEY) mode, which are highly sensitive to the valence state of Cu and Ni ions.<sup>[28]</sup> Figure 2j shows the Cu-L<sub>2,3</sub> sXAS spectra of CuO NWs/CF and Ni(OH)<sub>2</sub>/CuO NWs/CF together with CuO as a Cu<sup>2+</sup> reference and Cu<sub>2</sub>O as a Cu<sup>1+</sup> reference.<sup>[29]</sup> The single sharp peak at the Cu-L<sub>2,3</sub> sXAS spectra of both the CuO NWs/CF and Ni(OH)<sub>2</sub>/CuO NWs/CF electrodes can be attributed to the 2p<sup>5</sup>3d<sup>10</sup> final state at the same energy (931.3 eV) as that of CuO, indicating a Cu<sup>2+</sup> valence state. The observation of the Cu<sup>2+</sup> signal indicates very few layers of Ni(OH)<sub>2</sub> covering the CuO NWs since the TEY mode has a probing depth of ≈5 nm.<sup>[30]</sup> This also indicated that the Ni(OH)<sub>2</sub> nanosheets do not completely block the signal of the CuO nanowires in the hierarchical structure during the electrochemical reaction. The weak peak for Cu<sub>2</sub>O assigned to the 2p<sup>5</sup>3d<sup>10</sup>6s<sup>1</sup> final state locates<sup>[29]</sup> at nearly the same energy at Cu metal, which could not be detected further, thus confirming the presence of CuO NWs on the top of the Cu substrate. Figure 2k presents the Ni-L<sub>2,3</sub> sXAS spectra of Ni(OH)<sub>2</sub>/CuO NWs/CF together with NiO and Ni metal as references. The similar multiple spectral features and the energy position observed in the Ni-L<sub>2,3</sub> sXAS spectra of Ni(OH)<sub>2</sub>/CuO NWs/CF as those of NiO demonstrate a Ni<sup>2+</sup> valence state. The absence of a lower energy shoulder below the main peak excludes the Ni metal state. We also measured the Cu 2p XPS spectra of CuO NWs/CF and Ni 2p and Cu 2p XPS spectra of Ni(OH)<sub>2</sub>/CuO NWs/CF. The quantitative curve-fitted analysis reveals the 2+ valence state of Ni ion (Figure S11a, Supporting Information), and there is no obvious difference in valence states of Cu between the electrodes of CuO NWs/CF and Ni(OH)<sub>2</sub>/CuO NWs/CF (Figure S11b, Supporting Information).

The as-obtained electrodes were directly utilized as the working electrode for electrocatalytic performance evaluation. The electrochemical performance toward the UOR (electrolyte: 1 M KOH with 0.5 M urea) and OER (electrolyte: 1 M KOH) was evaluated through a conventional three-electrode configuration. The *i*R-compensated linear sweep voltammetry (LSV) curves of the series of catalysts for both water and urea oxidations were plotted. Remarkably, by adding 0.5 M urea to the alkaline solution, Cu NWs/CF, Cu(OH)<sub>2</sub> NWs/CF, and CuO NWs/CF electrodes exhibit obviously decreased potentials to reach desired

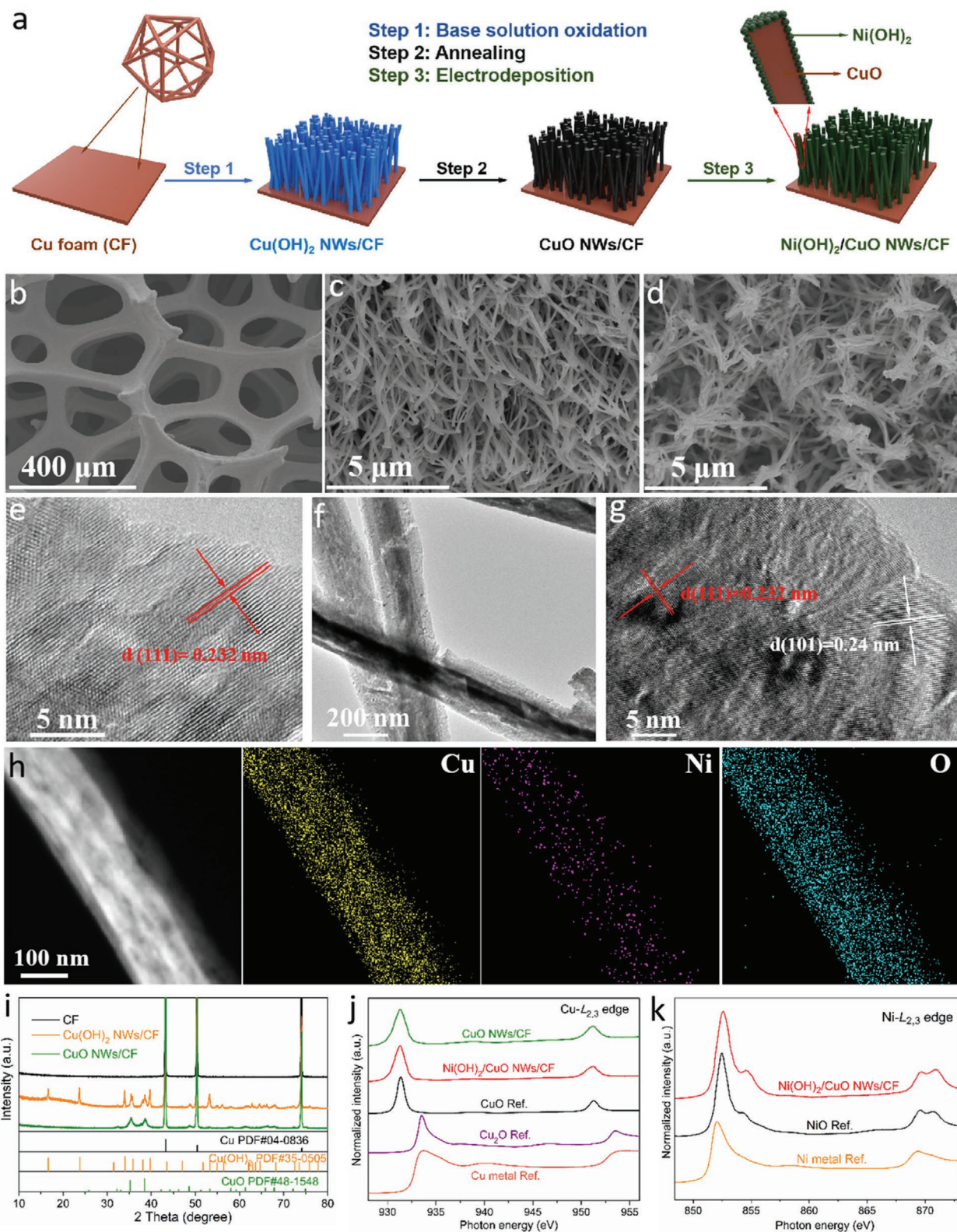


**Figure 2.** a) Schematic illustration for the steps involved in the synthesis of Ni(OH)<sub>2</sub>/CuO NWs/CF. SEM images of b) commercial CF, c) CuO NWs/CF, and d) Ni(OH)<sub>2</sub>/CuO NWs/CF. e) HRTEM images of CuO NWs/CF. f) TEM and g) HRTEM images of Ni(OH)<sub>2</sub>/CuO NWs/CF. h) HAADF-STEM and corresponding elemental mapping images of Ni(OH)<sub>2</sub>/CuO NWs/CF. i) XRD patterns of CF, Cu(OH)<sub>2</sub> NWs/CF, and CuO NWs/CF. Normalized sXAS spectra at the j) Cu-L<sub>2,3</sub> edge of CuO NWs/CF and Ni(OH)<sub>2</sub>/CuO NWs/CF and k) Ni-L<sub>2,3</sub> edge of Ni(OH)<sub>2</sub>/CuO NWs/CF together with different references.

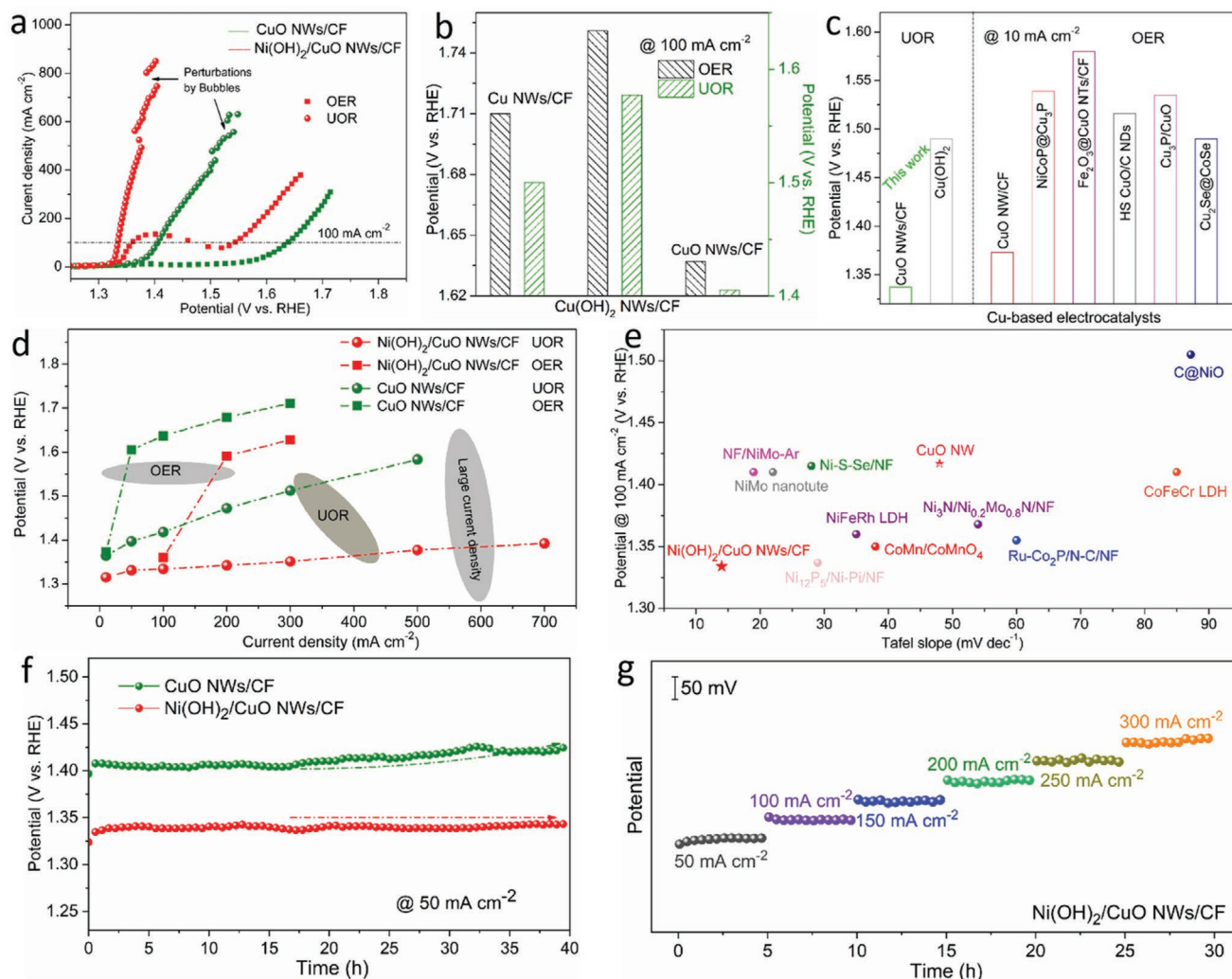


**Figure 3.** a) LSV curves toward OER and UOR of CuO NWs/CF and Ni(OH)<sub>2</sub>/CuO NWs/CF electrodes. b) Potential comparison of Cu NWs/CF, Cu(OH)<sub>2</sub> NWs/CF, and CuO NWs/CF electrodes for OER and UOR. c) Potential comparison of CuO NWs/CF electrode for OER and UOR with recently reported Cu-based electrocatalysts. d) Potential comparison of CuO NWs/CF and Ni(OH)<sub>2</sub>/CuO NWs/CF electrodes for OER and UOR. e) Comparison of potential corresponding to 100 mA cm<sup>-2</sup> and a Tafel slope with some reported UOR electrocatalysts. f) Chronopotentiometric curves of CuO NWs/CF and Ni(OH)<sub>2</sub>/CuO NWs/CF electrodes fixed at 50 mA cm<sup>-2</sup>. g) Multistep chronopotentiometry curve at different current densities from 50 to 300 mA cm<sup>-2</sup> for Ni(OH)<sub>2</sub>/CuO NWs/CF electrode.

current densities, especially for the CuO NWs/CF electrode (Figure 3a,b; Figure S12, Supporting Information), indicating that the UOR occurs preferentially over the OER. In particular, the LSV curves show that CuO NWs/CF has a distinct electrocatalytic activity for the UOR. For example, CuO NWs/CF requires a low potential of 1.405 V to reach a current density of 100 mA cm<sup>-2</sup> toward the UOR, which is 96 and 171 mV lower than that needed for the Cu NWs/CF and Cu(OH)<sub>2</sub> NWs/CF electrodes, respectively (Figure 3b). Of note, when a noble metal oxide, RuO<sub>2</sub>, was loaded on the electrode of CuO NWs/CF, the required potential to achieve 100 mA cm<sup>-2</sup> was 1.433 V (Figure S13, Supporting Information). This value is even higher than that of the bare CuO NWs/CF electrode (1.405 V), indicating highly active sites of CuO. The dramatically enhanced UOR activity of CuO NWs/CF is further confirmed by the decreased potential corresponding to a current density of 10 mA cm<sup>-2</sup>

when compared to the reported high-performance Cu-based OER electrocatalysts (e.g., 1.336 V toward UOR for Cu(OH)<sub>2</sub> NWs/CF catalyst and 1.535 V toward OER for Cu<sub>3</sub>P/CuO catalyst, Figure 3c; Table S1, Supporting Information). After the introduction of Ni(OH)<sub>2</sub>, the OER activity of Ni(OH)<sub>2</sub>/CuO NWs/CF is superior to that of CuO NWs/CF. The peak at ≈1.37 V is ascribed to the redox pair of Ni<sup>2+</sup>/Ni<sup>3+</sup>. Significantly, upon the presence of small concentrations of urea in alkaline media, the peak disappeared immediately, beyond which the oxidation current density increases rapidly (Figure S14, Supporting Information); this also demonstrated that the UOR occurs preferentially to OER. When compared to the OER, the UOR activity of Ni(OH)<sub>2</sub>/CuO NWs/CF shows a much lower potential to obtain higher current densities (Figure 3d). Remarkably, the Ni(OH)<sub>2</sub>/CuO NWs/CF electrode delivers exceptional UOR activity, demanding low potentials of only 1.334, 1.377, and

1.392 V at 100, 500, and 700 mA cm<sup>-2</sup>, respectively (Figure 3d). Additionally, the influence of electrodeposition times on the UOR activities was evaluated, and polarization curves demonstrate that Ni(OH)<sub>2</sub>-90 (the one denoted as Ni(OH)<sub>2</sub>/CuO NWs/CF) is superior to Ni(OH)<sub>2</sub>-60 and Ni(OH)<sub>2</sub>-120 (Figure S15, Supporting Information). Tafel plots are provided to unveil the reaction kinetics of the UOR and OER (Figure S16, Supporting Information). For the UOR process, the Ni(OH)<sub>2</sub>/CuO NWs/CF electrode has an exceptional low Tafel slope (14 mV dec<sup>-1</sup>) compared to that of the CuO NWs/CF electrode (48 mV dec<sup>-1</sup>). More importantly, the value of 14 mV dec<sup>-1</sup> is about an order of magnitude smaller than that required for the OER process (166 mV dec<sup>-1</sup>). The abovementioned results show that the rationally designed hierarchical Ni(OH)<sub>2</sub>/CuO NWs/CF electrode is a highly active catalyst toward the UOR. In terms of the potential at 100 mA cm<sup>-2</sup> and the Tafel slope toward the UOR, the Ni(OH)<sub>2</sub>/CuO NWs/CF electrode exhibits comparable and even superior activities to most of the recently reported UOR electrocatalysts (Figure 3e; Table S2, Supporting Information). Gas chromatography analysis was used to identify the gaseous product during the UOR process. Notably, negligible O<sub>2</sub> was detected during the reaction process, and the amounts of theoretically calculated gaseous product matched well with the experimentally measured N<sub>2</sub> gas over time, highlighting the high electrochemical selectivity toward UOR with a Faradaic efficiency of 99.0% (Figure S17, Supporting Information).

To assess the stability of the designed electrodes under the operating conditions, chronopotentiometry (CP) measurements were performed. Impressively, besides superior activity toward the UOR, the Ni(OH)<sub>2</sub>/CuO NWs/CF electrode also demonstrated exceptional stability with no observed potential increase during 40 h at a fixed current density of 50 mA cm<sup>-2</sup>, while the CuO NWs/CF electrode exhibited a gradual potential increase after 20 h during the testing (Figure 3f). Furthermore, the multistep chronopotentiometry curve was obtained to further evaluate the electrochemical performance, where the current density was increased from 50 to 300 mA cm<sup>-2</sup> with an increment of 50 mA cm<sup>-2</sup> per 5 h (Figure 3g). The corresponding potentials remained constant in each process, manifesting outstanding mass transport properties and robust stability of Ni(OH)<sub>2</sub>/CuO NWs/CF toward the UOR in the harsh alkaline solutions. After the UOR stability measurement, the structure, morphology, and composition of the CuO NWs/CF and Ni(OH)<sub>2</sub>/CuO NWs/CF electrodes were further examined. The XRD pattern of the CuO NWs/CF electrode after the stability test agrees with the precatalyst (electrode before the electrochemical reaction), demonstrating no phase change after the UOR test (Figure S18, Supporting Information). The activity degradation of the CuO NWs/CF electrode is mainly ascribed to the aggregation of nanowires (Figure S19a, Supporting Information). In contrast, the aggregation level for the Ni(OH)<sub>2</sub>/CuO NWs/CF electrode is much smaller than that of the CuO NWs/CF electrode, enabling exposure of active sites to the electrolytes (Figure S19b, Supporting Information). Moreover, the Ni(OH)<sub>2</sub>/CuO NWs/CF electrode also exhibits stable surface crystalline structures after the UOR, where no amorphous layer was observed (Figure S20, Supporting Information).

To track the origins of the outstanding UOR performance mentioned above, additional cyclic voltammetry (CV)

measurements were performed to analyze double-layer capacitance (C<sub>dl</sub>), a measure of electrochemical-active surface area (ECSA) and surface-active sites.<sup>[23a]</sup> Based on the CV curves (Figure S21, Supporting Information), the Ni(OH)<sub>2</sub>/CuO NWs/CF electrode has the highest C<sub>dl</sub> value of 0.36 F cm<sup>-2</sup>, which is ≈1.2 and ≈16.4 times higher than that of the CuO NWs/CF (0.29 F cm<sup>-2</sup>) and Cu(OH)<sub>2</sub> NWs/CF (0.022 F cm<sup>-2</sup>) electrodes, respectively. This confirms that the Ni(OH)<sub>2</sub>/CuO NWs/CF electrode has considerable surface-active sites, which lead to superior electrochemical activity. To highlight the advantage of the nanowire structure that exposes a large number of highly active species on the surface, cleaned commercial CF was directly calcined in air (CuO<sub>x</sub>/CF). Remarkably, there was an ≈46-fold increase of the C<sub>dl</sub> value and clearly improved UOR activity of CuO NWs/CF compared to CuO<sub>x</sub>/CF (Figure 4a; Figure S22, Supporting Information). In addition to the significantly improved active sites, the electrode kinetics were further evaluated by electrochemical impedance spectroscopy (EIS).<sup>[11f]</sup> The Ni(OH)<sub>2</sub>/CuO NWs/CF electrode possesses an ultralow charge-transfer resistance of ≈0.2 Ω, in contrast to the CuO NWs/CF (≈0.9 Ω), Cu(OH)<sub>2</sub> NWs/CF (≈1.7 Ω), and CF (≈5.0 Ω) (Figure 4b). The extremely low charge-transfer resistance of the Ni(OH)<sub>2</sub>/CuO NWs/CF electrode indicates a rapid charge-transfer property and fast catalytic kinetics, further promoting the UOR performance.

To explore the roles and contributions of CuO NWs and Ni(OH)<sub>2</sub> for electrocatalysis, the UOR activities and phase structures of Cu(OH)<sub>2</sub> NWs/CF, Cu<sub>2</sub>O NWs/CF, and Cu NWs/CF electrodes before and after UOR testing were evaluated. Under a fixed current density of 50 mA cm<sup>-2</sup>, the required potentials to achieve this value quickly decreased during the initial period (≈240 min) and became stable afterward for the Cu(OH)<sub>2</sub> NWs/CF electrode (Figure 4c, inset). Impressively, the UOR activity of the Cu(OH)<sub>2</sub> NWs/CF electrode greatly improved after testing compared to the initial activity (Figure 4c), along with significantly enhanced surface-active sites (Figure S23a–c, Supporting Information). Meanwhile, a surface phase transition from Cu(OH)<sub>2</sub> to CuO was also observed (Figure S23d, Supporting Information). Furthermore, we also studied the effects of low-valence states of Cu (Cu<sup>1+</sup> in Cu<sub>2</sub>O and Cu<sup>0+</sup> in metallic Cu) toward the UOR performance. Similarly, a partial surface phase transition from Cu<sub>2</sub>O and Cu to CuO, and improved UOR activity were observed for the Cu<sub>2</sub>O NWs/CF and Cu NWs/CF electrodes at the same time (Figures S24 and S25, Supporting Information). These results confirm that the electrochemical reaction-induced CuO phase is the most stable and active phase toward the UOR. However, the CuO NWs/CF electrode has a strong performance advantage compared to the phase-transformed Cu(OH)<sub>2</sub> NWs/CF, Cu<sub>2</sub>O NWs/CF, and Cu NWs/CF electrodes, highlighting the crucial role of the directly formed CuO phase. To assess the intrinsic activity, Ni(OH)<sub>2</sub> was electrodeposited on carbon cloth (CC) and CF. As exhibited in Figure 4d, the bare CC substrate shows negligible UOR activity. Ni(OH)<sub>2</sub>/CC meanwhile exhibits good UOR activity that requires only 1.368 V to achieve 50 mA cm<sup>-2</sup>, which is ≈250 mV less than that of the OER process (1.616 V). More specifically, the electrocatalytic selectivity toward the UOR of Ni(OH)<sub>2</sub> is confirmed by the high current efficiency value of nearly 100% (98.7%) at a potential of 1.43 V.<sup>[12]</sup> Importantly, Ni(OH)<sub>2</sub>/CC also

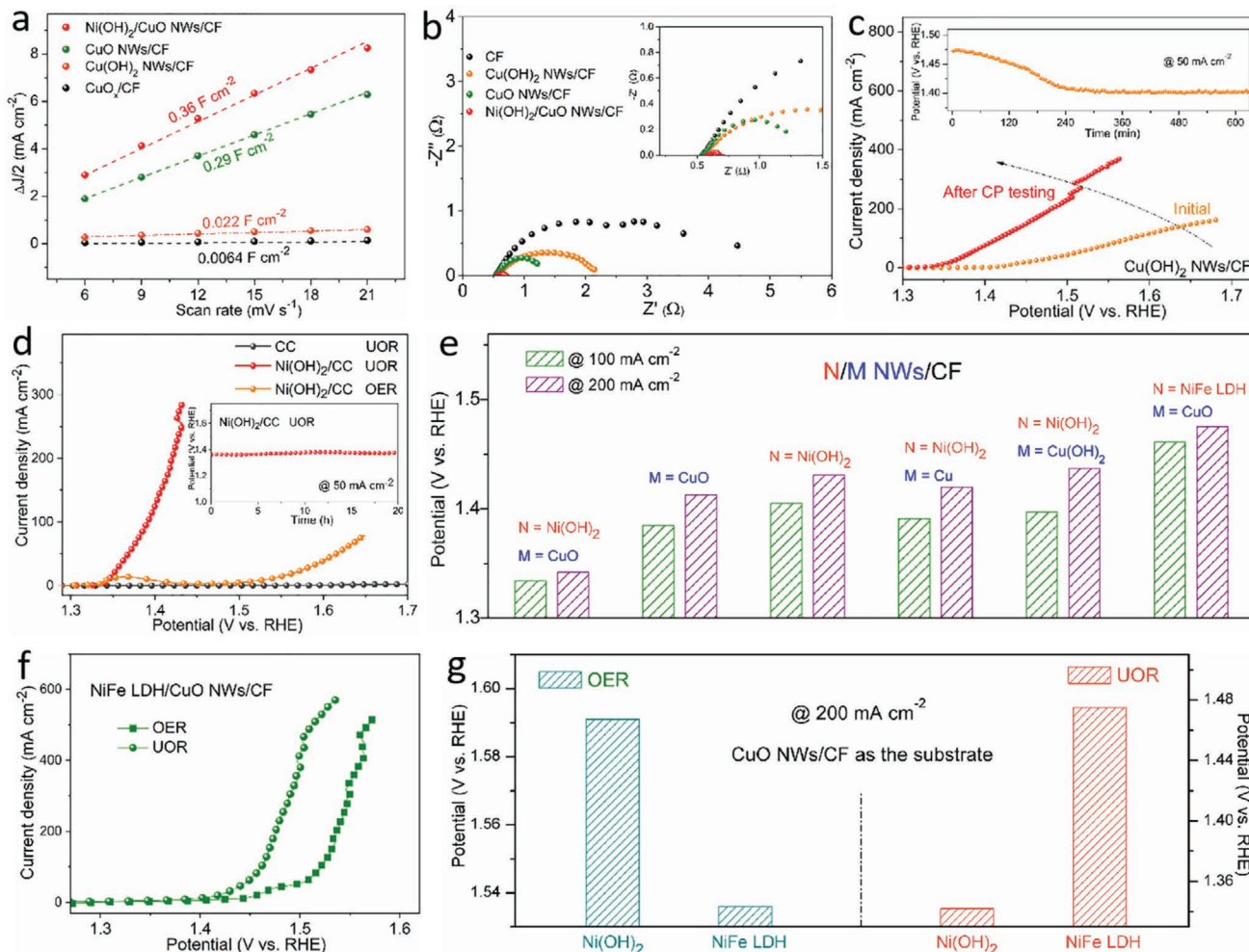


**Figure 4.** a) Dependence of current density on the scan rates for determination of the  $C_{dl}$ . b) Nyquist plots at 1.61 V ( $iR$ -uncorrected). c) LSV curves toward UOR of  $\text{Cu}(\text{OH})_2$  NWs/CF electrode before and after CP testing (inset: CP curve fixed at  $50 \text{ mA cm}^{-2}$ ). d) LSV curves toward UOR activities of CC and  $\text{Ni}(\text{OH})_2/\text{CC}$  and OER activity of  $\text{Ni}(\text{OH})_2/\text{CC}$  (inset: CP curve fixed at  $50 \text{ mA cm}^{-2}$  of  $\text{Ni}(\text{OH})_2/\text{CC}$  electrode for UOR). e) Potential (at 100 and  $200 \text{ mA cm}^{-2}$ ) comparisons of various designed electrodes to highlight the unique hierarchical structure of  $\text{Ni}(\text{OH})_2/\text{CuO}$  NWs/CF toward UOR. f) LSV curves toward OER and UOR activities of NiFe LDH/ $\text{CuO}$  NWs/CF. g) Potentials at  $200 \text{ mA cm}^{-2}$  of  $\text{Ni}(\text{OH})_2/\text{CuO}$  NWs/CF and NiFe LDH/ $\text{CuO}$  NWs/CF toward OER and UOR.

exhibits impressive UOR operational stability with a negligible potential increase during 20 h of testing (Figure 4d, inset). The high intrinsic UOR activity of  $\text{Ni}(\text{OH})_2$  was further confirmed by the UOR activity of  $\text{Ni}(\text{OH})_2/\text{CF}$  electrode, where CF substrate also exhibited low UOR activity (Figure S26, Supporting Information).

Next, a systematic experimental study examined the potential synergistic interplay between the hierarchical structure containing  $\text{CuO}$  NWs and  $\text{Ni}(\text{OH})_2$ .  $\text{Cu}$  NWs/CF and  $\text{Cu}(\text{OH})_2$  NWs/CF were selected as the substrates to electrodeposit  $\text{Ni}(\text{OH})_2$ . As shown in Figure 4e, though coupled with  $\text{Ni}(\text{OH})_2$ , the UOR activities of the  $\text{Ni}(\text{OH})_2/\text{Cu}$  NWs/CF and  $\text{Ni}(\text{OH})_2/\text{Cu}(\text{OH})_2$  NWs/CF electrodes were inferior to that of the  $\text{CuO}$  NWs/CF electrode mainly due to the low intrinsic UOR activities of  $\text{Cu}$  and  $\text{Cu}(\text{OH})_2$ . NiFe LDH was further electrodeposited on the surface of  $\text{CuO}$  NWs/CF for comparison. With the presence of urea in the alkaline solution, the UOR activity is also influenced by its competitive OER behavior. The high OER

activity of the NiFe LDH/ $\text{CuO}$  NWs/CF electrode is revealed by its clearly enhanced current densities at high potentials (Figure 4f). Of note, it was reported that when coupled with conductive  $\text{Cu}$  NWs, the current density of  $\text{Cu}@\text{NiFe}$  LDH was reported to exceed  $1000 \text{ mA cm}^{-2}$  at a potential of 1.55 V, highlighting the high intrinsic OER activity of NiFe LDH and the important role of the conductive substrate to OER.<sup>[23a]</sup> It is worth noting that among the studied electrodes, the NiFe LDH/ $\text{CuO}$  NWs/CF exhibited the poorest UOR activity, revealing by the highest potentials of 1.461 and 1.475 V to reach 100 and  $200 \text{ mA cm}^{-2}$ , respectively (Figure 4e). The unsatisfactory UOR activity of the NiFe LDH/ $\text{CuO}$  NWs/CF electrode is thus attributed to the high selectivity and activity toward the OER of NiFe LDH. The trends of OER and UOR activities of  $\text{Ni}(\text{OH})_2$  and NiFe LDH in Figure 4g are consistent with the adsorption energy properties in Figure 1f. The experimental data in Figure 4d demonstrated high activity, selectivity, and durability of  $\text{Ni}(\text{OH})_2$  toward the UOR. Thus, rationally integrating two

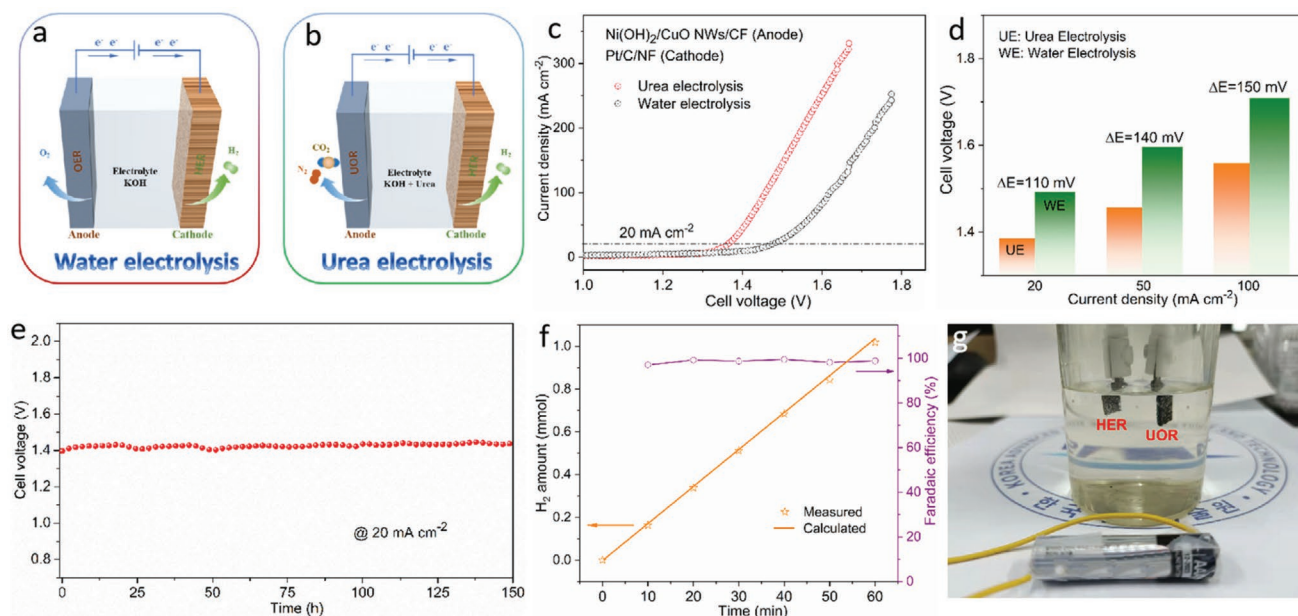


**Figure 5.** An illustration of a) a water electrolytic cell and b) urea electrolytic cell. c) LSV curves for the Ni(OH)<sub>2</sub>/CuO NWs/CF (anode)//Pt/C/NF (cathode) couple in 1 M KOH with and without 0.5 M urea. d) Comparison of cell voltage for urea electrolysis and water electrolysis systems at different current densities. e) Chronopotentiometry curves of Ni(OH)<sub>2</sub>/CuO NWs/CF (anode)//Pt/C/NF (cathode) coupled with a fixed current density of 20 mA cm<sup>-2</sup> tested in a two-electrode configuration for 150 h. f) Faradaic efficiency of H<sub>2</sub> production in the HER//UOR system upon operation time. g) A home-made electrolysis-water device driven by a commercial battery with an initial potential of 1.5 V in 1 M KOH with 0.5 M urea.

active species, including CuO and Ni(OH)<sub>2</sub>, successfully provides a synergistic effect that can realize exceptional high electrocatalytic UOR performance.

Encouraged by the exceptional UOR performance of the Ni(OH)<sub>2</sub>/CuO NWs/CF catalyst, a full urea electrolysis cell using Ni(OH)<sub>2</sub>/CuO NWs/CF electrode as an anode and Pt/C on Ni foam (Pt/C/NF) as a cathode (Figure S27, Supporting Information) was assembled in 1 M KOH and 0.5 M urea. Meanwhile, the overall water electrolysis performance using the same cathode and anode materials was also evaluated in 1 M KOH for comparison (Figure 5a,b). Noticeably, a cell voltage of only 1.38 V is required for urea electrolysis (HER and UOR) to achieve the current density of 20 mA cm<sup>-2</sup> (Figure 5c). In contrast, the traditional water electrolysis (HER and OER) requires a higher cell voltage of 1.49 V to reach the same current density (Figure 5c), suggesting that replacing OER with UOR at the anode is an effective strategy for energy-saving H<sub>2</sub> production (Figure 5d). Significantly, this outstanding activity positions the designed catalyst as the most active full urea electrolyzer in alkaline media (Table S3, Supporting Information). Moreover, the proposed system can deliver 20 mA cm<sup>-2</sup> at a cell voltage of ≈1.36 V for continuous testing of 150 h, demonstrating outstanding long-term running capability (Figure 5e). By quantifying the H<sub>2</sub> produced, the Faradaic efficiency for HER is calculated to be ≈100%, demonstrating an outstanding capability of Pt/C/NF//Ni(OH)<sub>2</sub>/CuO NWs/CF for H<sub>2</sub> production in the HER//UOR system (Figure 5f; Figure S28, Supporting Information). As a further demonstration, using a 1.5 V commercial dry battery as the energy source, the urea electrolyzer can also be driven, thus approaching the goal of efficient hydrogen production (Figure 5g). During the electrolysis process, the continuous generation of gas bubbles on the surface of the electrodes

confirms the high efficiency of the urea electrolyzer (Movie S1, Supporting Information).

### 3. Conclusion

We presented a facile approach to design a hierarchical structure containing metal oxides (CuO NWs) in situ formed from a commercial Cu foam substrate by a chemical oxidation process, and Ni(OH)<sub>2</sub> is further electrodeposited on the metal oxide surfaces. The 3D nanostructure enables exposure of a considerable amount of active sites, and the self-supported electrode ensures long-term high reactivity. CuO and Ni(OH)<sub>2</sub> are shown to be highly selective materials for the UOR over OER. Furthermore, CuO is identified as the most stable site for the electrochemical reaction. Moreover, a synergistic interaction between CuO NWs and Ni(OH)<sub>2</sub> also contributes to the exceptional activity. The as-obtained Ni(OH)<sub>2</sub>/CuO NWs/CF electrode exhibits outstanding UOR activity, affording a current density of 100 mA cm<sup>-2</sup> at 1.334 V and excellent catalytic durability in 1 M KOH and 0.5 M urea electrolyte. Furthermore, full urea electrolysis only requires a cell voltage of ≈1.36 V to deliver 20 mA cm<sup>-2</sup>, which is 0.13 V lower than that required for water splitting, along with robust long-term electrocatalytic durability for 150 h. This work further deepens the rational design and construction of hierarchical nanostructures for applications in energy electrocatalysis.

### Supporting Information

Supporting Information is available from the Wiley Online Library or from the author.

## Acknowledgements

H.S. and W.J. gratefully acknowledge the National Research Foundation of Korea (NRF) funded by the Ministry of Science, ICT (NRF-2017M3A7B4049547, NRF-2019R1A2C2006006, 2021M3H4A1A01079300) and KAIST Institute for the NanoCentury. J.L. and F.C. gratefully acknowledge the Research Grant Council of Hong Kong for support through the projects (Project Nos. 16201820 and 16206019). The authors acknowledge support from the Max Planck-POSTECH-Hsinchu Center for Complex Phase Materials.

## Conflict of Interest

The authors declare no conflict of interest.

## Author Contributions

H.S. and J.L. contributed equally to this work. W.J. and F.C. conceived the project and supervised the work. H.S. designed the experiments, conducted material synthesis, and performed electrochemical measurements. J.-M.C., S.-C.H., and Z.H. performed the soft XAS experiments and data analysis. H.K. and S.K. assisted with the experiments and structural characterization. J.L. and F.C. carried out DFT calculations. H.S. prepared the manuscript, and G.C. and W.J. helped to modify the manuscript. All authors discussed the results and commented on the manuscript.

## Data Availability Statement

The data that support the findings of this study are available from the corresponding authors upon reasonable request.

## Keywords

electrocatalysis, hierarchical structures, hydrogen production, oxygen evolution reaction, urea oxidation reaction

Received: August 27, 2021

Revised: November 1, 2021

Published online:

- [1] a) M. F. Lagadec, A. Grimaud, *Nat. Mater.* **2020**, *19*, 1140; b) Z. W. Seh, J. Kibsgaard, C. F. Dickens, I. Chorkendorff, J. K. Nørskov, T. F. Jaramillo, *Science* **2017**, *355*, eaad4998; c) K. Wang, K. Sun, Z. Li, Z. Lv, T. Yu, X. Liu, G. Wang, G. Xie, L. Jiang, *Electron. Mater. Lett.* **2020**, *16*, 164; d) C. Liu, C. Kong, F.-J. Zhang, C.-M. Kai, W.-Q. Cai, X.-Y. Sun, W.-C. Oh, *J. Korean Ceram. Soc.* **2021**, *58*, 135; e) H. Sun, S. Song, X. Xu, J. Dai, J. Yu, W. Zhou, Z. Shao, W. Jung, *Adv. Energy Mater.* **2021**, *11*, 2101937; f) H. Liu, S. Cao, J. Zhang, S. Liu, C. Chen, Y. Zhang, S. Wei, Z. Wang, X. Lu, *Mater. Today Phys.* **2021**, *20*, 100448.
- [2] a) C. Wei, R. R. Rao, J. Peng, B. Huang, I. E. L. Stephens, M. Risch, Z. J. Xu, Y. Shao-Horn, *Adv. Mater.* **2019**, *31*, 1806296; b) G. Chen, Y. Sun, R. R. Chen, C. Biz, A. C. Fisher, M. P. Sherburne, J. W. Ager III, J. Gracia, Z. J. Xu, *J. Phys. Chem. Lett.* **2021**, *3*, 031004.
- [3] a) Y. Zhou, H. J. Fan, *ACS Mater. Lett.* **2021**, *3*, 136; b) Z.-F. Huang, J. Song, S. Dou, X. Li, J. Wang, X. Wang, *Matter* **2019**, *1*, 1494; c) N. Ma, G. Chen, Y. Zhu, H. Sun, J. Dai, H. Chu, R. Ran, W. Zhou, R. Cai, Z. Shao, *Small* **2020**, *16*, 2002089; d) H. Sun, J. Dai, W. Zhou,

- Z. Shao, *Energy Fuels* **2020**, *34*, 10547; e) J. Gao, H. Tao, B. Liu, *Adv. Mater.* **2021**, *33*, 2003786; f) J. Yao, W. Huang, W. Fang, M. Kuang, N. Jia, H. Ren, D. Liu, C. Lv, C. Liu, J. Xu, Q. Yan, *Small Methods* **2020**, *4*, 2000494; g) B. Zhou, Y. Li, Y. Zou, W. Chen, W. Zhou, M. Song, Y. Wu, Y. Lu, J. Liu, Y. Wang, S. Wang, *Angew. Chem., Int. Ed.* **2021**, *60*, 22908.
- [4] a) H. Sun, X. Xu, Y. Song, W. Zhou, Z. Shao, *Adv. Funct. Mater.* **2021**, *31*, 2009779; b) L. Li, H. Sun, Z. Hu, J. Zhou, Y.-C. Huang, H. Huang, S. Song, C.-W. Pao, Y.-C. Chang, A. C. Komarek, H.-J. Lin, C.-T. Chen, C.-L. Dong, J.-Q. Wang, L. Zhang, *Adv. Funct. Mater.* **2021**, *31*, 2104746; c) L. An, C. Wei, M. Lu, H. Liu, Y. Chen, G. G. Scherer, A. C. Fisher, P. Xi, Z. J. Xu, C.-H. Yan, *Adv. Mater.* **2021**, *33*, 2006328; d) F. Yu, L. Yu, I. K. Mishra, Y. Yu, Z. F. Ren, H. Q. Zhou, *Mater. Today Phys.* **2018**, *7*, 121.
- [5] a) X. Sun, R. Ding, *Catal. Sci. Technol.* **2020**, *10*, 1567; b) Y. Li, J. Li, Q. Qian, X. Jin, Y. Liu, Z. Li, Y. Zhu, Y. Guo, G. Zhang, *Small* **2021**, *17*, 2008148.
- [6] a) B. Zhu, Z. Liang, R. Zou, *Small* **2020**, *16*, 1906133; b) L. Wang, Y. Zhu, Y. Wen, S. Li, C. Cui, F. Ni, Y. Liu, H. Lin, Y. Li, H. Peng, B. Zhang, *Angew. Chem., Int. Ed.* **2021**, *133*, 10671; c) S.-K. Geng, Y. Zheng, S.-Q. Li, H. Su, X. Zhao, J. Hu, H.-B. Shu, M. Jaroniec, P. Chen, Q.-H. Liu, S.-Z. Qiao, *Nat. Energy* **2021**, *6*, 904. d) A. Kumar, X. Liu, J. Lee, B. Debnath, A. R. Jadhav, X. Shao, V. Q. Bui, Y. Hwang, Y. Liu, M. G. Kim, H. Lee, *Energy Environ. Sci.* **2021**, <https://doi.org/10.1039/D1EE02603H>.
- [7] a) C. Wang, H. Lu, Z. Mao, C. Yan, G. Shen, X. Wang, *Adv. Funct. Mater.* **2020**, *30*, 2000556; b) L. Zhang, L. Wang, H. Lin, Y. Liu, J. Ye, Y. Wen, A. Chen, L. Wang, F. Ni, Z. Zhou, S. Sun, Y. Li, B. Zhang, H. Peng, *Angew. Chem., Int. Ed.* **2019**, *58*, 16820; c) L. Wang, Y. Zhu, Y. Wen, S. Li, C. Cui, F. Ni, Y. Liu, H. Lin, Y. Li, H. Peng, B. Zhang, *Angew. Chem., Int. Ed.* **2021**, *60*, 10577.
- [8] a) J. Wang, T. Liao, Z. Wei, J. Sun, J. Guo, Z. Sun, *Small Methods* **2021**, *5*, 2000988; b) M. Kuang, P. Han, L. Huang, N. Cao, L. Qian, G. Zheng, *Adv. Funct. Mater.* **2018**, *28*, 1804886; c) C. Feng, M. B. Faheem, J. Fu, Y. Xiao, C. Li, Y. Li, *ACS Catal.* **2020**, *10*, 4019; d) L. Yang, Z. Liu, S. Zhu, L. Feng, W. Xing, *Mater. Today Phys.* **2021**, *16*, 100292; e) J.-H. Yang, M. Chen, X. Xu, S. Jiang, Y. Zhang, Y. Wang, Y. Li, J. Zhang, D. Yang, *Appl. Surf. Sci.* **2021**, *560*, 150009.
- [9] a) J.-J. Zhang, W.-W. Bao, M.-Y. Li, C.-M. Yang, N.-N. Zhang, *Chem. Commun.* **2020**, *56*, 14713; b) Q. Li, N. Li, J. An, H. Pang, *Inorg. Chem. Front.* **2020**, *7*, 2089; c) J. S. Kim, B. Kim, H. Kim, K. Kang, *Adv. Energy Mater.* **2018**, *8*, 1702774; d) Y. Liu, G. Zhang, C. Zuo, K. Zhao, J. Zeng, J. Yin, H. Chen, S. Xie, Y. Qiu, *J. Electrochem. Soc.* **2020**, *167*, 116520.
- [10] a) X. Zhu, X. Dou, J. Dai, X. An, Y. Guo, L. Zhang, S. Tao, J. Zhao, W. Chu, X. C. Zeng, C. Wu, Y. Xie, *Angew. Chem., Int. Ed.* **2016**, *55*, 12465; b) G. Ma, Q. Xue, J. Zhu, X. Zhang, X. Wang, H. Yao, G. Zhou, Y. Chen, *Appl. Catal., B* **2020**, *265*, 118567; c) B. Xu, X. Yang, X. Liu, W. Song, Y. Sun, Q. Liu, H. Yang, C. Li, *J. Power Sources* **2020**, *449*, 227585.
- [11] a) M. Liu, Y. Jiao, S. Zhan, H. Wang, *Catal. Today* **2020**, *355*, 596; b) D. Liu, T. Liu, L. Zhang, F. Qu, G. Du, A. M. Asiri, X. Sun, *J. Mater. Chem. A* **2017**, *5*, 3208; c) T. Guo, X. Xu, X. Wang, J. Zhou, H. Wang, Z. Shi, M. Huang, *Chem. Eng. J.* **2021**, *417*, 128067; d) Q. Li, X. Li, J. Gu, Y. Li, Z. Tian, H. Pang, *Nano Res.* **2021**, *14*, 1405; e) L. Fei, H. Sun, R. Ran, W. Zhou, Z. Shao, *Ind. Eng. Chem. Res.* **2021**, *60*, 1185; f) A. Kumar, V. Q. Bui, J. Lee, A. R. Jadhav, Y. Hwang, M. G. Kim, Y. Kawazoe, H. Lee, *ACS Energy Lett.* **2021**, *6*, 354.
- [12] a) M. Zeng, J. Wu, Z. Li, H. Wu, J. Wang, H. Wang, L. He, X. Yang, *ACS Sustainable Chem. Eng.* **2019**, *7*, 4777; b) H. Jiang, M. Sun, S. Wu, B. Huang, C.-S. Lee, W. Zhang, *Adv. Funct. Mater.* **2021**, *31*, 2104951.
- [13] a) D. Zhou, P. Li, X. Lin, A. McKinley, Y. Kuang, W. Liu, W.-F. Lin, X. Sun, X. Duan, *Chem. Soc. Rev.* **2021**, *50*, 8790; b) X. Zhang,

- H. Wang, L. Shui, G. Zhou, X. Wang, R. Ma, J. Wang, *Sci. China Mater.* **2021**, *64*, 339; c) L.-F. Gu, C.-F. Li, J.-W. Zhao, L.-J. Xie, J.-Q. Wu, Q. Ren, G.-R. Li, *J. Mater. Chem. A* **2021**, *9*, 13279.
- [14] a) J. Wang, S. Choi, J. Kim, S. W. Cha, J. Lim, *Catalysts* **2020**, *10*, 770; b) L. Liang, K.-Y. Niu, L. Zhang, J. Tian, K. Zhou, X.-L. Wang, X.-M. Zhang, M. Hong, *ACS Appl. Nano Mater.* **2021**, *4*, 6135; c) H. Sun, W. Jung, *J. Mater. Chem. A* **2021**, *9*, 15506; d) R. Siavash Moakhar, S. M. Hosseini-Hosseinabad, S. Masudy-Panah, A. Seza, M. Jalali, H. Fallah-Arani, F. Dabir, S. Gholipour, Y. Abdi, M. Bagheri-Hariri, N. Riahi-Noori, Y.-F. Lim, A. Hagfeldt, M. Saliba, *Adv. Mater.* **2021**, *33*, 2007285.
- [15] a) Y. Wang, J. Liu, G. Zheng, *Adv. Mater.* **2021**, *33*, 2005798; b) Y. Wang, Y. Li, L. Ding, J. Ding, *Chem. Commun.* **2019**, *55*, 13562; c) D. T. Tran, H. T. Le, T. L. Luyen Doan, N. H. Kim, J. H. Lee, *Nano Energy* **2019**, *59*, 216.
- [16] K. Zeng, X. Zheng, C. Li, J. Yan, J.-H. Tian, C. Jin, P. Strasser, R. Yang, *Adv. Funct. Mater.* **2020**, *30*, 2000503.
- [17] a) M. Luo, W. Sun, B. B. Xu, H. Pan, Y. Jiang, *Adv. Energy Mater.* **2021**, *11*, 2002762; b) X. Xu, Y. Pan, L. Ge, Y. Chen, X. Mao, D. Guan, M. Li, Y. Zhong, Z. Hu, V. K. Peterson, M. Saunders, C.-T. Chen, H. Zhang, R. Ran, A. Du, H. Wang, S. P. Jiang, W. Zhou, Z. Shao, *Small* **2021**, *17*, 2101573.
- [18] a) D. Guan, W. Zhou, Z. Shao, *Small Sci.* **2021**, *1*, 2100030; b) W. Zhang, L. Cui, J. Liu, *J. Alloys Compd.* **2020**, *821*, 153542.
- [19] W. Ye, X. Guo, T. Ma, *Chem. Eng. J.* **2021**, *414*, 128825.
- [20] H. Sun, W. Zhang, J.-G. Li, Z. Li, X. Ao, K.-H. Xue, K. K. Ostrikov, J. Tang, C. Wang, *Appl. Catal., B* **2021**, *284*, 119740.
- [21] a) W. Yang, X. Yang, C. Hou, B. Li, H. Gao, J. Lin, X. Luo, *Appl. Catal., B* **2019**, *259*, 118020; b) S. Lu, M. Hummel, Z. Gu, Y. Wang, K. Wang, R. Pathak, Y. Zhou, H. Jia, X. Qi, X. Zhao, B. B. Xu, X. Liu, *ACS Sustainable Chem. Eng.* **2021**, *9*, 1703; c) Y. Tong, P. Chen, M. Zhang, T. Zhou, L. Zhang, W. Chu, C. Wu, Y. Xie, *ACS Catal.* **2018**, *8*, 1.
- [22] W. Fang, L. Huang, S. Zaman, Z. Wang, Y. Han, B. Y. Xia, *Chem. Res. Chin. Univ.* **2020**, *36*, 611.
- [23] a) L. Yu, H. Zhou, J. Sun, F. Qin, F. Yu, J. Bao, Y. Yu, S. Chen, Z. Ren, *Energy Environ. Sci.* **2017**, *10*, 1820; b) B. Wang, S. Jiao, Z. Wang, M. Lu, D. Chen, Y. Kang, G. Pang, S. Feng, *J. Mater. Chem. A* **2020**, *8*, 17202; c) P. M. Bodhankar, P. B. Sarawade, G. Singh, A. Vinu, D. S. Dhawale, *J. Mater. Chem. A* **2021**, *9*, 3180.
- [24] Y. Cao, T. Wang, X. Li, L. Zhang, Y. Luo, F. Zhang, A. M. Asiri, J. Hu, Q. Liu, X. Sun, *Inorg. Chem. Front.* **2021**, *8*, 3049.
- [25] P. A. Shinde, S. Park, N. R. Chodankar, S. Park, Y.-K. Han, A. G. Olabi, S. C. Jun, *Appl. Mater. Today* **2021**, *22*, 100951.
- [26] S.-Y. Lee, I.-S. Kim, H.-S. Cho, C.-H. Kim, Y.-K. Lee, *Appl. Catal., B* **2021**, *284*, 119729.
- [27] Q. Zhou, T.-T. Li, J. Qian, W. Xu, Y. Hu, Y.-Q. Zheng, *ACS Appl. Energy Mater.* **2018**, *1*, 1364.
- [28] a) M.-J. Huang, G. Deng, Y. Y. Chin, Z. Hu, J.-G. Cheng, F. C. Chou, K. Conder, J.-S. Zhou, T.-W. Pi, J. B. Goodenough, H.-J. Lin, C. T. Chen, *Phys. Rev. B* **2013**, *88*, 014520; b) Y.-Y. Chin, Z. Hu, Y. Shimakawa, J. Yang, Y. Long, A. Tanaka, L. H. Tjeng, H.-J. Lin, C.-T. Chen, *Phys. Rev. B* **2021**, *103*, 115149; c) H. Guo, Z. W. Li, L. Zhao, Z. Hu, C. F. Chang, C.-Y. Kuo, W. Schmidt, A. Piovano, T.-W. Pi, O. Sobolev, D. I. Khomskii, L. H. Tjeng, A. C. Komarek, *Nat. Commun.* **2018**, *9*, 43; d) H. Guo, Z. W. Li, C. F. Chang, Z. Hu, C.-Y. Kuo, T. G. Perring, W. Schmidt, A. Piovano, K. Schmalzl, H. C. Walker, H.-J. Lin, C. T. Chen, S. Blanco-Canosa, J. Schlappa, C. Schüßler-Langeheine, P. Hansmann, D. I. Khomskii, L. H. Tjeng, A. C. Komarek, *Sci. Rep.* **2020**, *10*, 18012. e) J. Park, J. Cho, *Angew. Chem., Int. Ed.* **2020**, *59*, 15314. f) H. Sun, W. Zhou, *Energy Fuels* **2021**, *35*, 5716.
- [29] L. H. Tjeng, C. T. Chen, S. W. Cheong, *Phys. Rev. B* **1992**, *45*, 8205.
- [30] S. Gota, M. Gautier-Soyer, M. Sacchi, *Phys. Rev. B* **2000**, *62*, 4187.